

Detection of Defects in Additively Manufactured Metallic Materials with Machine Learning of Pulsed Thermography Images

Pulsed Thermal Tomography Nondestructive Examination of Additively Manufactured Reactor Materials and Components

Nuclear Science and Engineering Division

About Argonne National Laboratory

Argonne is a U.S. Department of Energy laboratory managed by UChicago Argonne, LLC under contract DE-AC02-06CH11357. The Laboratory's main facility is outside Chicago, at 9700 South Cass Avenue, Argonne, Illinois 60439. For information about Argonne and its pioneering science and technology programs, see www.anl.gov.

Document availability

Online Access: U.S. Department of Energy (DOE) reports produced after 1991 and a growing number of pre-1991 documents are available free at OSTI.GOV (<http://www.osti.gov/>), a service of the U.S. Dept. of Energy's Office of Scientific and Technical Information

Reports not in digital format may be purchased by the public from the National Technical Information Service (NTIS):

U.S. Department of Commerce
National Technical Information Service
5301 Shawnee Rd
Alexandria, VA 22312
www.ntis.gov
Phone: (800) 553-NTIS (6847) or (703) 605-6000
Fax: (703) 605-6900
Email: **orders@ntis.gov**

Reports not in digital format are available to DOE and DOE contractors from the Office of Scientific and Technical Information (OSTI):

U.S. Department of Energy
Office of Scientific and Technical Information
P.O. Box 62
Oak Ridge, TN 37831-0062
www.osti.gov
Phone: (865) 576-8401
Fax: (865) 576-5728
Email: **reports@osti.gov**

Disclaimer

This report was prepared as an account of work sponsored by an agency of the United States Government. Neither the United States Government nor any agency thereof, nor UChicago Argonne, LLC, nor any of their employees or officers, makes any warranty, express or implied, or assumes any legal liability or responsibility for the accuracy, completeness, or usefulness of any information, apparatus, product, or process disclosed, or represents that its use would not infringe privately owned rights. Reference herein to any specific commercial product, process, or service by trade name, trademark, manufacturer, or otherwise, does not necessarily constitute or imply its endorsement, recommendation, or favoring by the United States Government or any agency thereof. The views and opinions of document authors expressed herein do not necessarily state or reflect those of the United States Government or any agency thereof, Argonne National Laboratory, or UChicago Argonne, LLC.

Detection of Defects in Additively Manufactured Metallic Materials with Machine Learning of Pulsed Thermography Images

Pulsed Thermal Tomography Nondestructive Examination of Additively Manufactured Reactor Materials and Components

prepared by
Alexander Heifetz¹, Xin Zhang^{1,2}, Jafar Saniie², William Cleary³

¹Nuclear Science Engineering Division, Argonne National Laboratory

²Department of Electrical and Computer Engineering, Illinois Institute of Technology, Chicago, IL

³Fuel Fabrication Facility, Westinghouse Electric Company, Columbia, SC

September 15, 2020

Table of Contents

Table of Contents	1
List of Figures	2
Abstract	3
1. Introduction	4
2. Pulsed Thermography Imaging of Imprinted Defects	7
2.1. Development of additively manufactured metallic specimens	7
2.2. Pulsed thermography imaging system	8
3. Machine Learning Algorithms for Thermography Image Analysis	10
3.1. Spatial-Temporal Blind Source Separation (STBSS) Algorithm	10
3.1.1. Wavelet Transform spatial de-noising	11
3.1.2. Neural Learning-based Blind Source Separation (NLBSS) algorithm	12
3.2. Spatial-Temporal Sparse Dictionary Learning (STSDL) Algorithm	12
3.2.1. Wavelet Transform spatial de-noising	13
3.2.2. Singular Value Decomposition	13
3.2.3. Sparse Dictionary Learning (SDL)	14
4. Benchmarking of Machine Learning Algorithms Performance	16
5. Conclusions	20
References	21

List of Figures

Figure 1 – Overview of LPBF: (a) Step 1 prepares the powder bed (b) Fabrication occurs in Step 2 where porosity can be introduced into AM metallic parts due to incomplete melting of powder particles or insufficient overlapping of melt pools.	4
Figure 2 – (Top) 3D rendering of hemispherical porosity defects imprinted in AM specimens. (Bottom) Design pattern of hemispherical defects of different diameters and depths relative to plate surface (all dimensions are in mm).....	7
Figure 3 – Photograph of two SS-316L and one INC718 plates manufactured with LPBF method	8
Figure 4 – (Top) Schematics of flash thermography setup. (Bottom) Experimental laboratory setup.	9
Figure 5 – Flowchart of the STBSS algorithm.	11
Figure 6 – Flowchart of the STSDL algorithm.	13
Figure 7 – Visualization of ICA, PCA, BSS, STBSS, SDL and STSDL algorithms performance in detection of pattern of large imprinted defects in SSH16 (high porosity), SSL316L (low porosity), and INC718 specimens.	16
Figure 8 – Visualization of ICA, PCA, BSS, STBSS, SDL and STSDL algorithms performance in detection of pattern of small imprinted defects in SSH16 (high porosity), SSL316L (low porosity), and INC718 specimens.	17
Figure 9 – Benchmarking of ICA, PCA, NLBSS, STBSS, SDL, and STSDL algorithms performance in detection of imprinted flaws in SSH36 (high porosity), SSL316 (low porosity), and INC718 specimens. The larger and smaller defect patterns contain a total of 12 and 20 imprinted defects, respectively. Performance of the algorithms was ranked by the F-score (values between 0 and 1) and execution run time (measured in seconds). The largest value of F-score for each AM specimen and defect pattern is indicating by highlighting (color on-line).	18

Abstract

Additive manufacturing (AM) is an emerging method for cost-efficient fabrication of nuclear reactor parts. AM of metallic structures for nuclear energy applications is currently based on laser powder bed fusion (LPBF) process, which can introduce internal material flaws, such as pores and anisotropy. Integrity of AM structures needs to be evaluated nondestructively because material flaws could lead to premature failures due to exposure to high temperature, radiation and corrosive environment in a nuclear reactor. Quality control (QC) requires nondestructive evaluation (NDE) of actual AM structures. Pulsed thermography is a potentially promising QC technique because it is scalable to arbitrary structure size. However, detection sensitivity of this method is limited by noises. We investigate separation of signal from noise in thermography images using several machine learning (ML) methods, including new spatio-temporal blind source separation (STBSS) and spatio-temporal sparse dictionary learning (STSDL) methods. Performance of the ML methods is benchmarked using thermography data obtained from imaging stainless steel 316L and Inconel 718 specimens produced LPBF method with imprinted calibrated porosity defects. The ML methods are ranked by F-score and execution runtime. The ML methods with higher accuracy require longer run time. However, this runtime is sufficiently short to perform QC within a realistic time frame.

1. Introduction

Additive manufacturing (AM) is an emerging method for cost-efficient production of low-volume custom and unique parts with minimal supply-chain dependence [1]. In particular, AM potentially provides a cost-saving option for replacing aging nuclear reactor parts and reducing costs for new construction of advanced reactors [2]. Metals of interest for passive structures in nuclear applications typically include high-strength corrosion-resistant stainless steel alloys, such as stainless steel 316/316L (SS316L). Because of high strength (200GPa Young's modulus at room temperature), shape forming of these metals into complex geometry structures is not trivial. AM of such metals, which have melting range 1370°C to 1430°C, is currently based on laser powder-bed fusion (LPBF) process [3,4]. Basic schematics of LPBF process are shown in Figure 1. Because of the intrinsic features of LPBF, e.g. Marangoni convection, material defects such as porosity and anisotropy can appear in the metallic structure [5]. Porosity can be introduced into AM parts due to incomplete melting of the powder particles or insufficient overlapping of the melt pools [6]. Oscillations in the surface of the melt pool caused by rapid heating and cooling result in powder ejection and splattering of the melt, resulting in surface roughness and porosity [7-9].

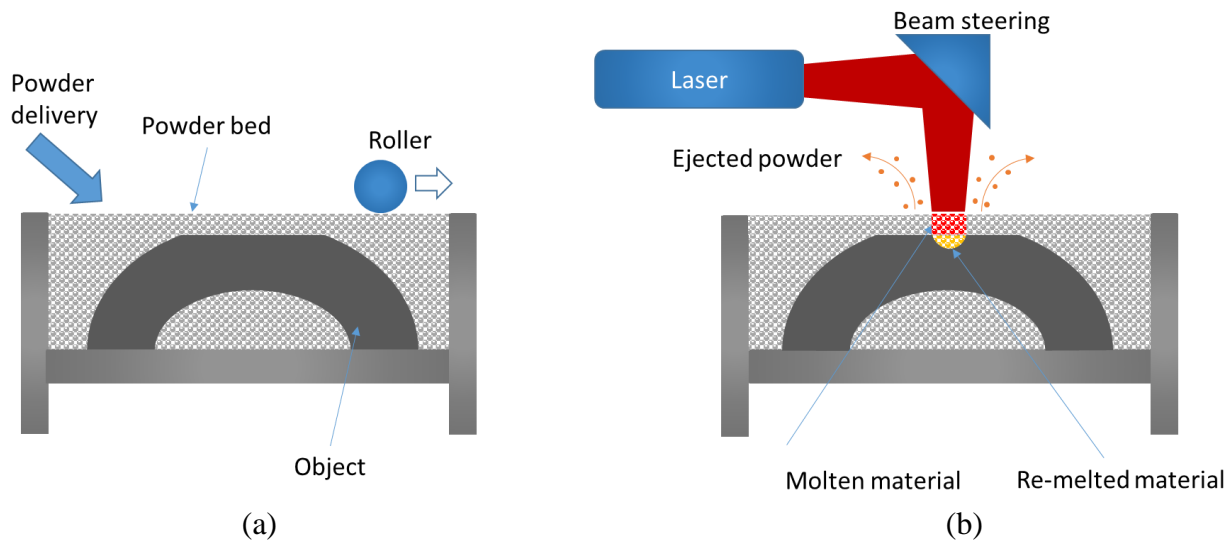


Figure 1 – Overview of LPBF: (a) Step 1 prepares the powder bed (b) Fabrication occurs in Step 2 where porosity can be introduced into AM metallic parts due to incomplete melting of powder particles or insufficient overlapping of melt pools.

Because reproducibility in AM is currently lower than that of conventional manufacturing, each structure needs to be examined nondestructively before deployment in an environment with high safety requirements, such as inside a nuclear reactor. Presence of porosity material defects could potentially combine with fatigue of AM metallic structure [10,11] due to long-term exposure to high temperature and ionizing radiation to decrease structure service life. In addition, corrosion damage to AM metallic structures from long term exposure to high-temperature reactor coolant fluids could be accelerated by corrosion front encountering sub-surface porosity material defects

[12,13]. Quality control (QC) in AM involves detection of material flaws in real-time during manufacturing, and non-destructive evaluation (NDE) of the structure after manufacturing [14]. Recently, machine learning (ML) has been explored for improving reliability of various stages in the AM process [15-18]. The objective of this report is to study the application of unsupervised ML to enhance capability of inspecting a structure in post-manufacturing.

During manufacturing, material flaws can, in principle, can be detected using X-ray radiography [19] or thermography [20]. In real-time monitoring, thermography measures blackbody radiation due to the heat of the build with an infrared (IR) imaging camera. Relative variation of the temperature in the image could be attributed to material flaws. However, because of high variance in the temperature due to unsteady-state heat conduction and aberrations in thermal images due to ejected un-sintered powder covering the fused metallic structure, real-time flaw detection with thermography is non-trivial. Applications of X-ray radiography to both real-time monitoring and post-manufacturing NDE are limited because of complex shape and lack of symmetry of AM structures. In post-manufacturing NDE, X-ray computed tomography can be used for high-resolution imaging of small coupons shaped in body-of-revolution symmetry form (spheres or cylinders). However, this provides sampled information about the quality of the AM process, but not about the actual structure. For post-manufacturing NDE, techniques involving contact probes, such ultrasonic testing, face challenges because AM structures have rough surfaces which affect probe coupling. In addition, high-resolution ultrasonic tomography requires time-consuming point-by-point raster scanning of specimens.

Pulsed thermography imaging potentially provides a number of advantages for NDE of AM structures in QC because the method is non-contact, one sided, and scalable to arbitrary size structures [21]. Because information is recorded as an image with a megapixel camera, the amount of mechanical scanning is significantly reduced compared to raster scan imaging with a single probe. Flash thermography utilizes a high intensity flash lamp to rapidly heat surface of sample, and a fast-frame megapixel infrared (IR) camera to capture data of spatial surface temperature distribution $T(x,y)$. The acquired data cube consists of a stack of surface temperature images taken at different times, $T(x,y,t)$. Information about material internal structure is contained in surface temperature transients because thermal resistance of internal structures affects local surface temperature decay rate. For example, low density pores have lower thermal diffusivity compared to the rest of the solid material. This results in slower surface temperature decay in regions above the defects, and appearance of local temperature “hot spots.” Information obtained from thermography measurements is relative but can be converted to absolute scale through calibration. In one approach, reconstruction of 3D thermal effusivity $e(x,y,z)$ can be obtained from the data cube $T(x,y,t)$ [22]. In another approach, as discussed in this paper, temperature data cube can be analyzed with advanced algorithms to detect material flaws [23-25]. Because thermography can be used for in-service inspection and NDE of AM parts, thermographic imaging 3D data can be used for construction of a *digital twin* for monitoring of integrity of AM structures.

QC based on flash thermography NDE depends on detection sensitivity, which is limited by experimental noises, such as imaging camera thermal noise, non-uniform illumination of the

specimen with the flash lamp. In addition, because detection of flaws is based on heat diffusion, contrast of “hot spots” is reduced due to blurring. In this paper, we investigate separation of signal from noise to enhance material flaw detection in thermography images using several machine learning (ML) methods. Performance of the ML methods is evaluated using the data cube obtained from flash thermography imaging of AM specimens. The specimens used in this study are SS-316L and INC718 plates produced with LPBF method, which contain imprinted calibrated porosity defects of various sizes. The ML methods developed and demonstrated in this paper are Spatial-Temporal Blind Source Separation (STBSS) and Spatial-Temporal Sparse Dictionary Learning (STSDL). The STBSS method is developed by combining wavelet-based de-noising with neural learning-based Blind Source Separation (NLBSS) algorithm. The NLBSS method developed recently for ML of thermography images, is based on combining the principal component analysis (PCA) and independent component analysis (ICA), which is implemented as a two-layer neural network. The STSDL method is similarly developed by combining wavelet-based de-noising with the sparse dictionary learning (SDL) method. Performance of the ML methods, as well as the previously developed NLBSS, and established PCA, ICA and SDL methods in detection of flaws in flash thermography data is ranked by F-score and algorithm execution runtime. Results of this paper indicate that STBSS and STSDL outperform existing methods in their capability of defects detection, albeit at the expense of increased runtime. However, the time to perform flash thermography measurements and ML analysis of images is sufficiently short for implementation of these methods in a realistic QC procedure.

2. Pulsed Thermography Imaging of Imprinted Defects

2.1. Development of additively manufactured metallic specimens

A set of two SS-316L and one INC718 plates was fabricated with LPBF method using EOS metal 3D printer. Fabrication of SS-316L and INC718 plates was based on 20 μ m and 40 μ m powder layers, respectively. The dimensions of the plates are Length \times Width \times Thickness: 152mm \times 76mm \times 10mm. The same pattern of calibrated defects consisting of hemispherical porosity regions containing un-sintered metallic powder were imprinted into the SS-316L and INC718 plates. The defects were imprinted during fabrication using an STL (stereolithography) file with a drawing of the pattern of hemispherical inclusions. In one of the SS-316L plate (SSH316) and the INC718 plate, defects consisted of 100% porosity (high porosity). In another SS-316L plate (SSL316) speed and power of the laser were adjusted to yield approximately 40% porosity in the defect regions (low porosity).

A computer rendering of the pattern of defects is shown in Figure 2 (top panel). A drawing with labels showing diameters and depths of the imprinted defects is provided in Figure 2 (bottom panel). Note that there are two patterns of defects on the plate: one with diameters $\phi = 5, 6$ and 8mm and depths $d = 2, 3, 4$, and 5mm, and another one with diameters $\phi = 1, 2, 3$, and 4mm and depths $d = 1, 2, 3, 4$ and 5mm. The diameters of defects decrease along the lines parallel to the longer side of the plate, while the depth along these lines is held constant. Along the lines parallel to the shorter side of the plate, the depth increases, while the diameter is fixed along these lines.

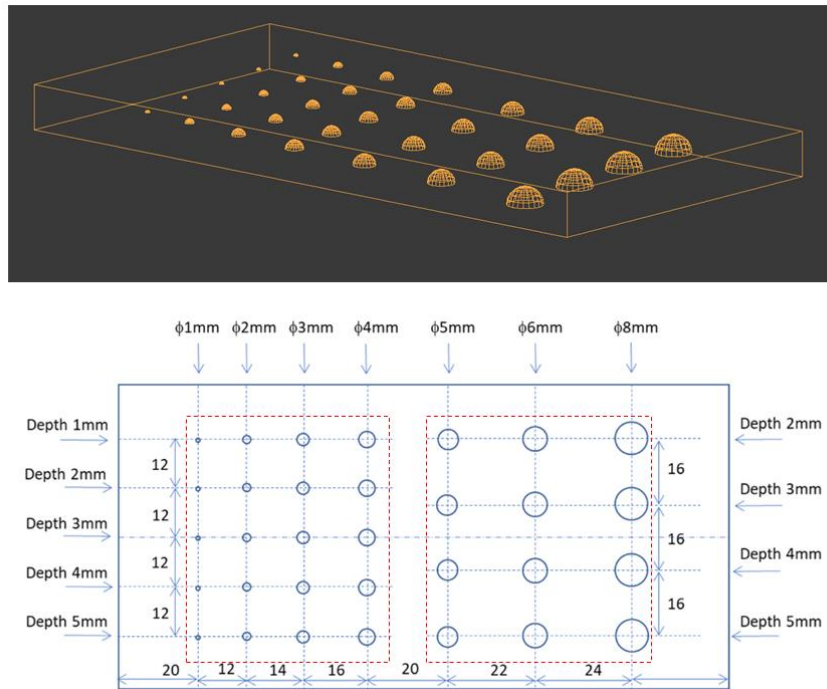


Figure 2 – (Top) 3D rendering of hemispherical porosity defects imprinted in AM specimens. (Bottom) Design pattern of hemispherical defects of different diameters and depths relative to plate surface (all dimensions are in mm)

Figure 3 shows the photograph of two SS-316L and one INC718 plates used in this study. The plates are visibly smooth on both sides.

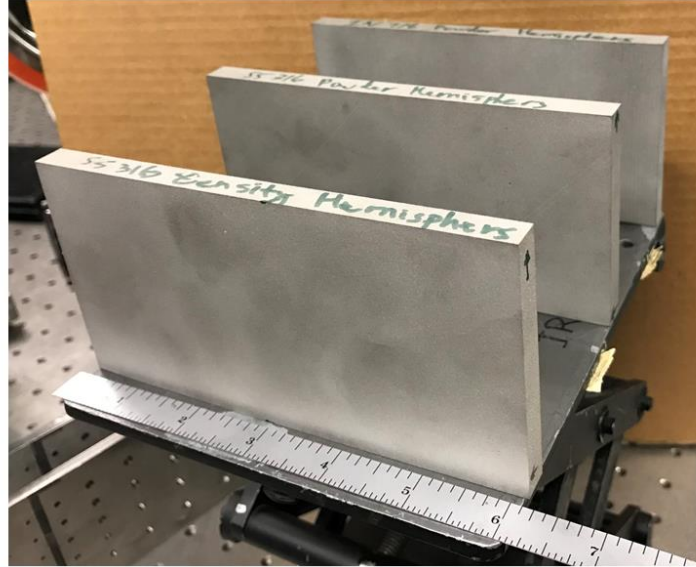


Figure 3 – Photograph of two SS-316L and one INC718 plates manufactured with LPBF method

2.2. Pulsed thermography imaging system

A schematic depiction of the flash thermography setup is shown in Figure 4 (top panel), with the photograph of the laboratory system displayed in Figure 4 (bottom panel). The method consists of illuminating material with white light flash lamp, which rapidly deposits heat on the material surface. In the experiment, a Balcar ASYM 6400 white light flash lamp delivers 6400MW of power in approximately 2ms duration flash. A pulse trigger sends a signal to capacitor to discharge in a circuit containing white light flash lamp. A megapixel fast frame infrared (IR) camera records time-resolved images of surface temperature distribution $T(x,y,t)$. The acquired thermal-imaging data cube therefore consists of a series of 2D images of the sample's surface temperature at consecutive time instants. The laboratory setup uses a FLIR X8501sc mid-wave infrared (MWIR) imaging camera, operating in 3-5 μ m band with noise equivalent temperature difference (NETD) of 20mK. X8501sc model provides maximum spatial resolution of 1280x1024, with frame rate at full window of 181Hz. The frame rate can be increased at the expense of reducing the viewing window. IR camera settings for all measurements in this study were 576x520 pixels window and 216Hz frame rate.

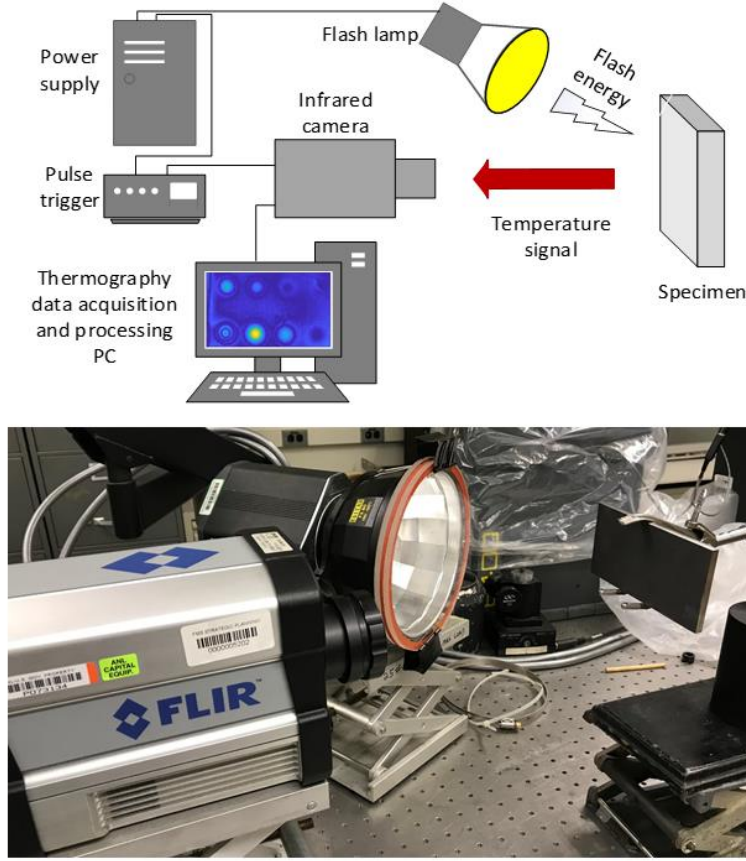


Figure 4 – (Top) Schematics of flash thermography setup. (Bottom) Experimental laboratory setup.

The two SS-316L and INC718 specimens were imaged with the plates positioned so that the spherical side of the internal defects was oriented towards the IR camera. For better absorption of thermal energy, all specimens were spay-painted with washable graphite paint. Two sets of flash thermography measurements were taken for each specimen. In one set of measurements, the section of each plate containing the “larger” defects was imaged (total of 12 imprinted defects), as can be seen in the right side of Figure 2 (bottom). In another set of measurements, sections of each plate containing the “smaller” defects pattern were imaged, as can be seen on the left side of Fig. 1(b) (total of 20 imprinted defects). Imaged area of the plate per measurement is approximately 76mm×76mm. The plates were imaged with FLIR X8501sc IR camera with 576x520 pixels window at 216Hz resolution rate. The time to acquire thermography data cube for each measurement was estimated from [22]

$$t = d^2 / \pi \alpha, \quad (1)$$

Where d is the thickness of the plate and α is material thermal diffusivity. Using the values of $d=10\text{mm}$, $\alpha=3.529\text{mm}^2/\text{s}$ for SS-316L [26] and $\alpha=3.019\text{mm}^2/\text{s}$ for INC718 [27] at room temperature, we obtain $t=9\text{s}$ for SS-316L and $t=10.5\text{s}$ for INC718 specimens, respectively.

3. Machine Learning Algorithms for Thermography Image Analysis

Efficiency of QC depends on the ability to detect material flaws in thermographic images. Raw images obtained from flash thermography typically suffer from low visibility contrast of subtle features with low signal to noise ratio (SNR). This typically occurs in flash thermography images because of thermal noises, non-uniform illumination of specimen with flashlight, insufficient noise equivalent temperature difference (NETD) sensitivity threshold of the IR camera, and blurring of features due to diffusion-based imaging. In this paper, we investigate extraction of low SNR features corresponding to material defects in thermal images using unsupervised ML algorithms, including new STBSS and STSDL methods. Unsupervised ML aims to learn potential patterns in unlabeled datasets, with minimal human supervision [28]. Common algorithms used in unsupervised learning are clustering analysis [29] and latent variable models learning [30]. Clustering analysis, such as hierarchical clustering, k-means clustering, is used to group datasets with the same attributes into one cluster. For latent variable models learning, including the PCA [31], expectation maximization (EM) algorithm and blind source separation (BSS) [32], the approach is to learn latent features that are not directly observed but inferred from observed datasets. The objective of PCA is to extract principal features of datasets by reconstructing new basis vectors to reduce information redundancy, which follows the same learning pattern as the unsupervised representation learning [33]. The unsupervised representation learning, such as SDL and ICA aim to identify the underlying explanatory features hidden in observed data. BSS aims to separate each latent source signal which shares the same attributes from mixed signals, and combines the representation learning with clustering analysis to enhance the performance.

3.1. Spatial-Temporal Blind Source Separation (STBSS) Algorithm

The STBSS approach is based on previously developed neural learning based blind source separation (NLBSS) [25]. The improvement of the new method described in this paper is achieved by introducing spatial de-noising with wavelet transform [34]. NLBSS algorithm, which combines PCA and fast ICA to enhance defect detection in time and space by separating defects from background and identifying the presence of defects [18]. PCA is a commonly used ML method for dimensionality reduction and feature extraction, which is applied for thermography defects detection as principal component thermography (PCT) [35]. ICA is another frequently used

method for separating a multivariate signal into additive subcomponents. Figure 4 shows the flow chart of STBSS algorithm, the schematics of which are discussed in the sub-sections below.

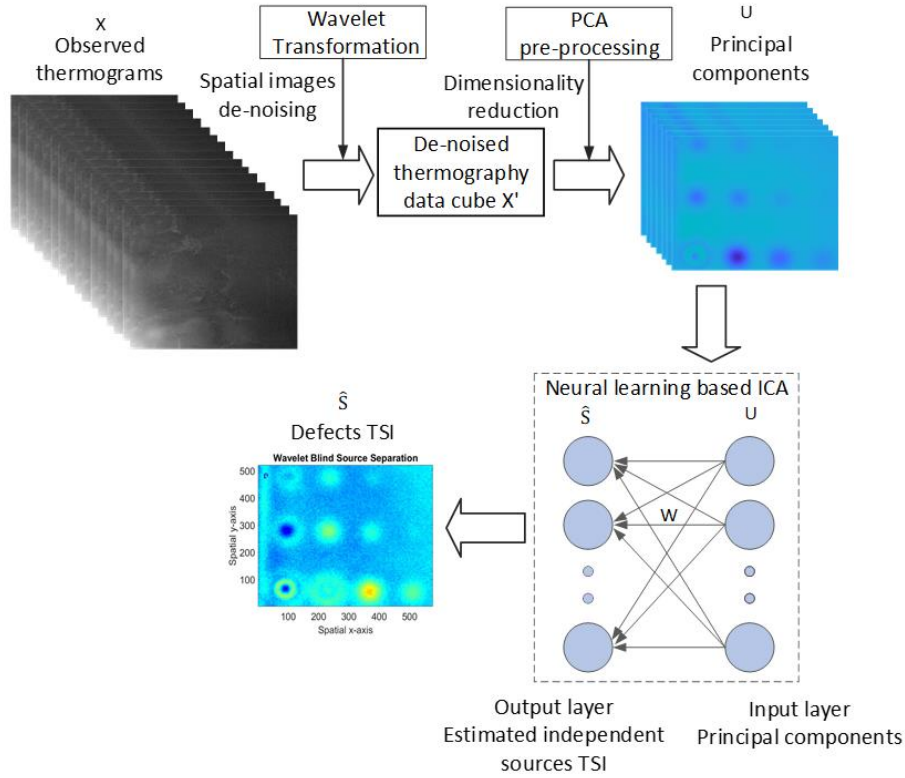


Figure 5 – Flowchart of the STBSS algorithm.

3.1.1. Wavelet Transform spatial de-noising

Wavelet transform is used to reduce the high-frequency thermography image noises in spatial-domain. These noises are random variation of brightness or color information in images and normally include the Additive White Gaussian Noises (AWGN), which can be efficiently reduced by using the wavelet transformation [36]. Wavelet transforms are mathematical methods to perform signal analysis when signal frequency changes over time. For image signals, the wavelet analysis selects the appropriate frequency band adaptively, then analyzes and filters abrupt changes in images, such as AWGN, to improve the image resolution.

As shown in Figure 5, wavelet transformation is applied to de-noise image noises for each observed thermography images X to obtain data cube X' . The flash thermography data cube can be written as $X \in R^{m \times n \times l}$, where l is the number of images (time frames), and each image has $m \times n$ pixels. Each image of the 3D data cube X is decomposed using wavelet transformation into four images with size $m \times n$, which includes one reconstruction image and three high-pass wavelet images. We keep the reconstruction images to form a new thermography data cube $X' \in R^{m \times n \times l}$, and discard the high-pass wavelet images which contain most image noise. In this study we apply the two-level Biorthogonal wavelet transformation implemented with the 'bior3.5' wavelet filter,

which has advantages of filtering image noises with minimal impact on image contrast gradients. In the numerical experiments, the filter was implemented using MATLAB library of wavelet filters.

3.1.2. Neural Learning-based Blind Source Separation (NLBSS) algorithm

In NLBSS, we use PCA [37] to extract principal features of thermography data, thus reducing thermal imaging noises and artifacts. As shown in Fig. 4, PCA is used to pre-process images X' to obtain principal components U . Next, U become inputs to the neural learning-based ICA [25] to estimate independent source signals \hat{S} , which are the thermal sources images (TSI) of defects. the ICA [38], implemented in a two-layer neural network structure, is applied to automatically separate image regions containing signatures of material defects from image regions which do not contain any material flaws. W is the estimation matrix for separating the mixed thermograms into TSIs of defects. The ICA is implemented in a neural network structure, which is composed of densely connected input layer (thermograms U), and an output layer (estimated source signal \hat{S}). The input layer has 50 neurons, equal to the number of principal components. The output layer has 12 neurons, equal to the number of independent components. Nonlinearity function 'pow3' ($g(u) = u^3$) [38] is used as the activation function to optimize training for robust convergence. Next, we use the reverse entropy [38] as the objective function to measure the non-Gaussian. We train this two-layer neural network with 100 epochs to estimate the TSI of defects. The neural network structure utilizes the fast fixed-point algorithm [38] for optimization to speed up detection of features in thermography images.

3.2. Spatial-Temporal Sparse Dictionary Learning (STSDL) Algorithm

The STSDL approach is based on sparse dictionary learning (SDL) method. SDL is a representation learning method which aims to find the sparse representation of the data. The new method STSDL consists of three stages of feature extraction to enhance defects detection for weak defect signals: wavelet transform, singular value decomposition (SVD), and SDL. Figure 6 shows the flow chart of the STSDL algorithm, the schematics of which are discussed in sub-sections below.

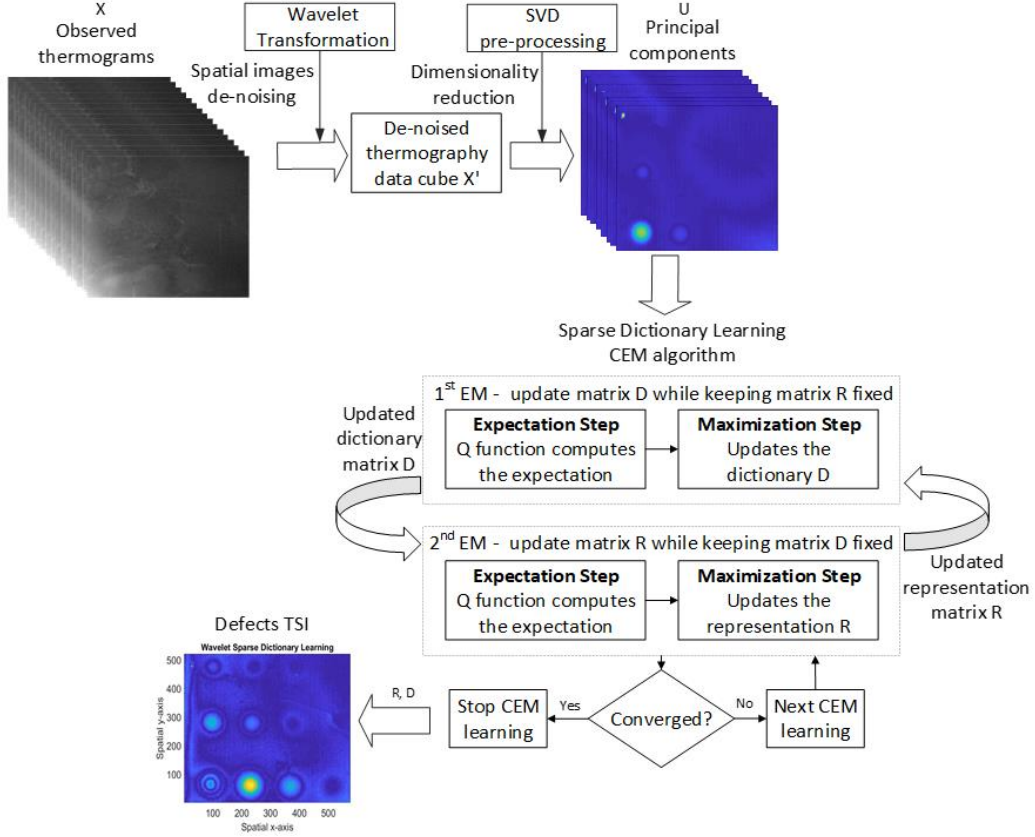


Figure 6 – Flowchart of the STSDL algorithm.

3.2.1. Wavelet Transform spatial de-noising

As shown in Figure 6, in the 1st stage of feature extraction, we apply the two-level Biorthogonal wavelet transformation implemented with the 'bior3.5' wavelet filter, which has advantages of filtering image noises with minimal impact on image contrast gradients. The details of wavelet transform implementation are the same as described in Section 3.1.1. The output of the wavelet filter is de-noised thermography data cube $X' \in R^{m \times n \times l}$, where there are l images, each having $m \times n$ pixels.

3.2.2. Singular Value Decomposition

We use the Singular Value Decomposition (SVD) to extract principal features of defect information for the 2nd stage feature extraction, as shown in Figure 6. Defects features are compressed in time-domain by reconstructing orthogonal thermography features to ameliorate thermal imaging experimental artifacts, such as uneven heating and image noises. The equation implementing SVD is

$$Y_{M \times N} = U_{M \times N} H_{N \times N} V_{N \times N}^T. \quad (2)$$

To apply Equation (2) to 3D thermography data cube $X' \in R^{m \times n \times l}$ obtained with Biorthogonal wavelet transformation described in Section 3.2.1, we reshape the array of $m \times n$ pixels in each

image into a single vector of length $M=m \cdot n$. The condensed 2D data is stored in matrix Y , where M and N represent the number of rows and columns, respectively ($N=l$ is the renamed number of recorded thermography frames). U and V are orthogonal matrices separately containing variability of data and time information. H is the matrix containing the singular values of Y . Thus, by decomposing the thermography data Y with SVD, the matrix U is constructed with orthogonal basis vectors which describe the largest variability in the data using the first few columns (N_l) of U . We use only few basis vectors of U , which contain principal features of data, as input for SDL to enhance detection of flaws.

3.2.3. Sparse Dictionary Learning (SDL)

SDL method aims to find the sparse representation of data by searching for the optimized basis vectors of dictionary. The dictionary includes the optimized basis vectors called atoms, which are linearly combined to represent defect information. Compared to BSS method, SDL allows more flexibility in sparse representation of defects information the atoms are not required to be orthogonal. In this study, we use the SDL to optimize the representation of data and further enhance extraction of features in thermography images corresponding to material defects. The objective function of the SDL algorithm is modeled as

$$\underset{R,D}{\text{minimize}} \ \|U - (RD')\|_1 + \frac{\gamma_r}{2} \|R\|_2^2 + \frac{\gamma_d}{2} \|D\|_2^2. \quad (3)$$

In Equation (3), U is the matrix consisting of the 2D data matrix obtained with SVD. The matrices D and R are the dictionary matrix and representation matrix, respectively. Thus, the first term in Equation (3) that measures the difference between U and (RD') models the reconstruction error, which is minimized to reduce information loss by forcing the algorithm to yield an optimal representation of the thermography data. Here the difference is measured with L_1 norm (linear norm) which gives more robust convergence compared with L_2 norm (squared norm). The second term imposed the constraint of sparse representation. Here γ_r is a scaling constant that determines the tradeoff between the reconstruction error and representation sparsity. The third term constrains atoms in dictionary from reaching arbitrarily high values resulting in low values of R . In the third term in Equation (3), γ_d is a scaling penalty constant. The second and third terms are regularized by L_2 norm to ensure sparsity and convergence for optimization.

Direct solution of the minimization problem in Equation (3) is computationally expensive since the Laplace distribution is not smooth. To circumvent this issue, a two-level hierarchical form of the Laplacian distribution is used [39]. The conditional expectation maximization (CEM) algorithm is utilized to iteratively search for D , R , while de-correlating the dependency between D and R . Therefore, in each CEM iteration there are two expectation maximization (EM) steps, which consist of updating D while keeping R fixed, and updating R while keeping D fixed. Matrix $T = [t_{ij}] \in R^{m \times n}$ is introduced as exponential prior for each pre-processed element u_{ij} to represent the missed data, and $\delta = [R, D]$ represents the parameters to be estimated. The constants γ_d and

γ_r are hyperparameters for fine-tuning optimization. Then, in one EM step, we apply the Q function to estimate the dictionary matrix D while keeping the representation matrix R known:

$$Q(D|\hat{\delta}) = E_T[\log p(D|\hat{R}, U, T) | U, \hat{\delta}]. \quad (4)$$

The Q function computes the expectation of the complete-data log-posterior regarding the missed data T , given the current estimates of parameters $\hat{\delta} = [\hat{R}, \hat{D}]$ in Equation (4).

To solve Equation (4), we apply the Bayes's rule, take log on both sides and remove terms which are irrelevant to parameter D . Then the complete-data log-posterior $\log p(D|U, T)$ is represented as

$$\log p(U|D, \hat{R}, T) + \log p(D) = -\frac{1}{2} \sum_i^m \sum_j^n [t_{ij}^{-1} (u_{ij} - \hat{r}_i' d_j)^2] - \frac{\gamma_d}{2} \sum_j^n d_j' d_j + C. \quad (5)$$

In Equation (5), C is a constant which does not depend on D and R . The posterior expectation of t_{ij}^{-1} is computed for the (expectation) E-step based on the observation that t_{ij}^{-1} follows the inverse Gaussian distribution. Then in the (maximization) M-step, we update the parameter estimate d_j in each row of D by maximizing the Q function shown in Equation (4). Next the partial derivative of the Q function with respect to d_j is set to zero, and we obtain closed-form update equation

$$d_j = (\hat{R}' \Omega_j \hat{R} + \gamma_d I_\theta)^{-1} \hat{R}' \Omega_j u_{.j}. \quad (6)$$

In equation (6), $\Omega_j = \text{diag} \{ (t_{1j}^{-1}), \dots, (t_{mj}^{-1}) \}$, $\theta_{ij} = u_{ij} - (rd')_{ij}$, and $u_{.j}$ is the j^{th} column of U . In the next EM step, we update matrix R while keeping matrix D fixed by following the same procedure described above. The closed-form update equation is

$$r_i = (\hat{D}' \Lambda_i \hat{D} + \gamma_r I_\theta)^{-1} \hat{D}' \Lambda_i u_{.i}. \quad (7)$$

In equation (7), $\Lambda_i = \text{diag} \{ (t_{i1}^{-1}), \dots, (t_{in}^{-1}) \}$ and $u_{.i}$ is the i^{th} row of U . Then, the convergence criteria is set as

$$\frac{\| (RD')^i - (RD')^{i-1} \|_2}{\| U \|_2} \leq \varepsilon. \quad (8)$$

Here L_2 normalization is used for calculating the convergence criteria, where ε is the threshold set to be $\varepsilon = 5 \times 10^{-3}$. If the convergence criterion is satisfied, which means that the difference between old and new values from SDL reconstruction is small, then parameters R and D are used to further extract features from thermography data to enhance defects detection. Otherwise, we apply the CEM algorithm for the next iteration to update parameters R and D .

4. Benchmarking of Machine Learning Algorithms Performance

Performance of ML algorithms in extracting features corresponding material flaws in images was evaluated using flash thermography data. Visualization of ML performance results in flaw detection in images is presented in Figure 7 and Figure 8. A total of 36 images is shown in Figure 7 and Figure 8. Data was obtained from measurements performed on SSH316 (high porosity defects), SSL316 (low porosity defects), and INC718 specimens. Separate thermography measurements were performed for large defects (see Figure 7) and small defects patterns (see Figure 8) in all plates, for a total of six measurements. In both Figures 7 and 8, there are six rows, with the labels indicating the types of ML algorithms used in the analysis. There are three columns in each figure, with labels indicating the types of AM specimen used in the corresponding flash thermography measurement. For baseline comparison, we include commonly used ICA, PCT, and recently developed NLBSS. Performance of STBSS algorithm, described in Section 3.1, is compared to the preceding three methods. Next, for baseline comparison, performance of SDL algorithm is shown. This is followed by demonstration of results obtained with the new STSDL algorithm described in Section 3.2.

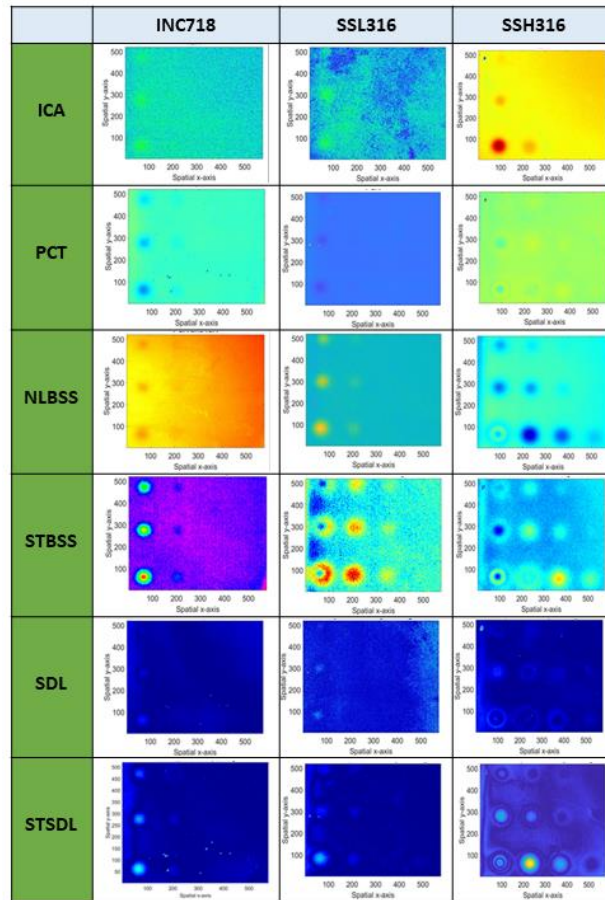


Figure 7 – Visualization of ICA, PCA, BSS, STBSS, SDL and STSDL algorithms performance in detection of pattern of large imprinted defects in SSH16 (high porosity), SSL316L (low porosity), and INC718 specimens.

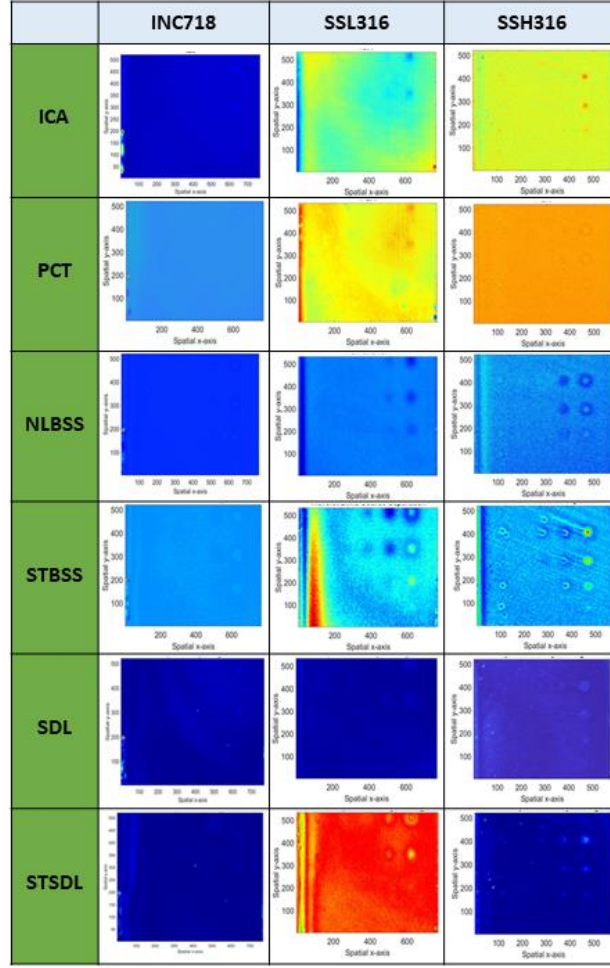


Figure 8 – Visualization of ICA, PCA, BSS, STBSS, SDL and STSDL algorithms performance in detection of pattern of small imprinted defects in SSH16 (high porosity), SSL316L (low porosity), and INC718 specimens.

Results of benchmarking ML algorithms performance using F-score and execution runtime are shown in Figure 9. The F-score, which is a measure of test accuracy, indicates how well the ML algorithms separate true signal from noise. There were 12 imprinted “larger” defects and 20 imprinted “smaller” defects. The F-score is proportional to how many defects from the total set of imprinted defects were detected. The values of the F-score are between 0 and 1, with the higher number indicating better accuracy. The F-scores in Figure 9 were calculated as

$$F_{score} = \frac{(\beta + 1) \times (Precision \times Recall)}{\beta^2 \times (Precision + Recall)}, \quad (9)$$

$$Precision = T_p / (T_p + F_p) \text{ and } Recall = T_p / (T_p + F_n). \quad (10)$$

Here T_p = true positive, F_p = false positive, F_n = false negative, β is the tradeoff (relative) parameter which determines if *Precision* or *Recall* is more important. In this study $\beta = 1$, which means *Precision* and *Recall* are equally important.

	ICA		PCT		NLBSS		STBSS		SDL		STSDL	
	Detected defects Diameter,depth (ϕ , d) mm		Detected defects Diameter,depth (ϕ , d) mm		Detected defects Diameter,depth (ϕ , d) mm		Detected defects Diameter,depth (ϕ , d) mm		Detected defects Diameter,depth (ϕ , d) mm		Detected defects Diameter,depth (ϕ , d) mm	
	F-score	Time	F-score	Time	F-score	Time	F-score	Time	F-score	Time	F-score	Time
Larger defects SSH316 12 Defects	($\phi 8$, d2), ($\phi 8$, d3) ($\phi 6$, d2), ($\phi 5$, d2)		($\phi 8$, d2), ($\phi 8$, d3) ($\phi 8$, d4), ($\phi 6$, d2) ($\phi 6$, d3)		($\phi 8$, d2), ($\phi 8$, d3) ($\phi 8$, d4), ($\phi 8$, d5) ($\phi 6$, d2), ($\phi 6$, d3) ($\phi 5$, d2), ($\phi 5$, d3)		($\phi 8$, d2), ($\phi 8$, d3) ($\phi 8$, d4), ($\phi 8$, d5) ($\phi 6$, d2), ($\phi 6$, d3) ($\phi 6$, d4), ($\phi 5$, d2) ($\phi 5$, d3), ($\phi 5$, d4)		($\phi 8$, d2), ($\phi 8$, d3) ($\phi 8$, d4), ($\phi 8$, d5) ($\phi 6$, d2), ($\phi 6$, d3) ($\phi 6$, d4), ($\phi 5$, d2) ($\phi 5$, d3)		($\phi 8$, d2), ($\phi 8$, d3) ($\phi 8$, d4), ($\phi 8$, d5) ($\phi 6$, d2), ($\phi 6$, d3) ($\phi 6$, d4), ($\phi 6$, d5) ($\phi 5$, d2), ($\phi 5$, d3) ($\phi 5$, d4)	
	0.5	52	0.59	7	0.8	10	0.91	112	0.86	14	0.96	130
Larger defects SSL316 12 Defects	($\phi 8$, d2), ($\phi 6$, d2)		($\phi 8$, d2), ($\phi 6$, d2) ($\phi 5$, d2)		($\phi 8$, d2), ($\phi 6$, d2) ($\phi 5$, d2), ($\phi 8$, d3) ($\phi 6$, d3)		($\phi 8$, d2), ($\phi 8$, d3) ($\phi 8$, d4), ($\phi 6$, d2) ($\phi 6$, d3), ($\phi 6$, d4) ($\phi 5$, d2), ($\phi 5$, d3) ($\phi 5$, d4)		($\phi 8$, d2), ($\phi 6$, d2) ($\phi 5$, d2)		($\phi 8$, d2), ($\phi 8$, d3) ($\phi 6$, d2), ($\phi 6$, d3) ($\phi 5$, d2), ($\phi 5$, d3)	
	0.29	100	0.4	7	0.59	12	0.86	133	0.4	14	0.67	74
Larger defects INC718 12 Defects	($\phi 8$, d2), ($\phi 6$, d2) ($\phi 5$, d2)		($\phi 8$, d2), ($\phi 6$, d2) ($\phi 5$, d2)		($\phi 8$, d2), ($\phi 6$, d2) ($\phi 5$, d2)		($\phi 8$, d2), ($\phi 8$, d3) ($\phi 6$, d2), ($\phi 6$, d3) ($\phi 5$, d2), ($\phi 5$, d3)		($\phi 8$, d2), ($\phi 6$, d2) ($\phi 5$, d2)		($\phi 8$, d2), ($\phi 8$, d3) ($\phi 6$, d2), ($\phi 6$, d3) ($\phi 5$, d2), ($\phi 5$, d3)	
	0.4	57	0.4	8	0.4	10	0.67	86	0.4	22	0.67	75
Smaller defects SSH316 20 Defects	($\phi 4$, d1), ($\phi 3$, d1) ($\phi 2$, d1)		($\phi 4$, d1), ($\phi 3$, d1) ($\phi 2$, d1)		($\phi 4$, d1), ($\phi 3$, d1) ($\phi 2$, d1), ($\phi 4$, d2) ($\phi 3$, d2), ($\phi 2$, d2)		($\phi 4$, d1), ($\phi 3$, d1) ($\phi 2$, d1), ($\phi 4$, d2) ($\phi 3$, d2), ($\phi 2$, d2) ($\phi 4$, d3), ($\phi 1$, d1)		($\phi 4$, d1), ($\phi 3$, d1) ($\phi 2$, d1), ($\phi 4$, d2) ($\phi 3$, d2), ($\phi 2$, d2) ($\phi 4$, d3)		($\phi 4$, d1), ($\phi 3$, d1) ($\phi 2$, d1), ($\phi 4$, d2) ($\phi 3$, d2), ($\phi 2$, d2) ($\phi 4$, d3)	
	0.26	58	0.26	7	0.46	9	0.57	116	0.52	15	0.52	106
Smaller defects SSL316 20 Defects	($\phi 4$, d1), ($\phi 3$, d1)		($\phi 4$, d1), ($\phi 3$, d1)		($\phi 4$, d1), ($\phi 3$, d1) ($\phi 2$, d1), ($\phi 4$, d2) ($\phi 3$, d2), ($\phi 2$, d2)		($\phi 4$, d1), ($\phi 3$, d1) ($\phi 2$, d1), ($\phi 4$, d2) ($\phi 3$, d2), ($\phi 2$, d2) ($\phi 4$, d3), ($\phi 3$, d3)		($\phi 4$, d1), ($\phi 3$, d1) ($\phi 2$, d1), ($\phi 4$, d2) ($\phi 3$, d2)		($\phi 4$, d1), ($\phi 3$, d1) ($\phi 2$, d1), ($\phi 4$, d2) ($\phi 3$, d2), ($\phi 2$, d2)	
	0.18	66	0.18	7	0.46	10	0.57	62	0.4	17	0.46	72
Smaller defects INC718 20 Defects	($\phi 4$, d1), ($\phi 3$, d1)		($\phi 4$, d1), ($\phi 3$, d1)		($\phi 4$, d1), ($\phi 3$, d1) ($\phi 2$, d1)		($\phi 4$, d1), ($\phi 3$, d1) ($\phi 2$, d1)		($\phi 4$, d1), ($\phi 3$, d1) ($\phi 2$, d1)		($\phi 4$, d1), ($\phi 3$, d1) ($\phi 2$, d1), ($\phi 4$, d2)	
	0.18	64	0.18	7	0.26	9	0.26	108	0.26	27	0.33	116

Figure 9 – Benchmarking of ICA, PCA, NLBSS, STBSS, SDL, and STSDL algorithms performance in detection of imprinted flaws in SSH36 (high porosity), SSL316 (low porosity), and INC718 specimens. The larger and smaller defect patterns contain a total of 12 and 20 imprinted defects, respectively. Performance of the algorithms was ranked by the F-score (values between 0 and 1) and execution run time (measured in seconds). The largest value of F-score for each AM specimen and defect pattern is indicating by highlighting (color on-line).

The runtime of algorithms in Figure 9 is measured in seconds. Detected defects for each entry in Figure 9 are listed as a set of numbers (ϕ , d), where ϕ is the defect diameter and d is its depth, all measured in mm (see Figs. 1 and 2). All benchmarking studies were performed on Intel (R) Core (TM) i7-8750H, CPU@2.20GHz 2.21GHz computer with 16GB RAM.

In general, internal defects with smaller diameter and deeper location are more difficult to detect. The reason is that defects of smaller size have smaller thermal resistance visible on the plate surface because heat can diffuse around these defects. In addition, thermal resistance of defects located deeper below the surface manifests itself when surface temperature has decayed to

the level close to the ambient temperature. These factors result in low thermal contrast “hot spots” on the specimen surface, which are difficult to detect. Further improvements in flash thermography hardware and ML algorithms would be needed to detect smaller and deeper-located defects. When comparing the materials, detection is generally better for SSH316, followed by SSL316 and INC718. This can be understood from the fact that SS316 has higher thermal diffusivity than INC718, and from higher thermal resistance contrast in high porosity SSH316 compared to low porosity SSL316.

The STBSS and STSDL methods have similar performance results, which is better than those of other ML algorithms considered in this study. The F-score of STBSS is slightly better for smaller defects, while the F-score of STSDL is slightly better for larger defects. The increase in accuracy is accomplished at the expense of increasing run time. For both STBSS and STSDL the runtime can be on the order of 100s. This is the time to process images for material section with dimensions of approximately 76mm×76mm×10mm. Additional time of approximately 10s to acquire images with flash thermography should be added to estimate the total time. For a structure with dimensions of 22.8cm×22.8cm×10mm, for example, the total processing time would be approximately 1000s or approximately 17min. In principle, this reasonable time for implementing QC for low-volume AM of structures. Processing time can be further reduced by using more powerful computing resources.

5. Conclusions

Additive manufacturing (AM) offers the potential of reduced-cost manufacturing of structures for nuclear energy applications. Laser powder bed fusion (LPBF) is a common method for AM of stainless steel 316L (SS316L) and similar high-strength corrosion-resistant metals and alloys used for passive structures in nuclear energy application. However, common defects appearing in structures manufactured with LPBF include porosity regions. Quality control of AM structures is needed before their deployment in the harsh environment of a nuclear reactor. In this paper, we have investigated application of ML image analysis algorithms to QC of metallic structures produced with LPBF method. The ML images were applied to flash thermography data obtained from NDE of SS316L and IN718 specimens with imprinted calibrated porosity defects. Two novel ML approaches were introduced to enhance detection of weak signals, the STBSS and STSDL. The former method consists of using wavelet transform de-noising, orthogonal decomposition of data with PCA, and separation of defects with ICA. The latter method also uses wavelet transform de-noising, but non-orthogonal data decomposition with SDL. Results of application of ML algorithms to thermography data indicate that, in general, smaller defects are detectable when they are located closer to the surface. STBSS and STSDL have similar performance, with STBSS showing slightly higher sensitivity in detection of smaller defects. Both STBSS and STSDL have better sensitivity in detection compared to other ML algorithms considered in this study. However, the increase in sensitivity is associated with increase in runtime. Nevertheless, the run time is sufficient to enable QC of low-volume AM of structures. Further enhancement in sensitivity of detection of defects will be investigated using a microscopic lens to achieve higher number of pixels per image of flaws. Future work will involve utilizing non-linear machine learning algorithms, such as Sparse PCA, ISOMAP, and deep representation learning [30], such as the convolutional neural network, auto-encoders, to efficiently extract features from thermography images.

References

1. T. DebRoy, H.L. Wei, J.S. Zuback, T. Mukherjee, J.W. Elmer, J.O. Milewski, A.M. Beese, A. Wilson-Heid, A. De, W. Zhang, “Additive manufacturing of metallic components – Process, structure and properties,” *Progress in Material Science* 92, 112-224 (2018).
2. X. Lou and D. Gandy, “Advanced manufacturing for nuclear energy,” *JOM* 71, 2834-2836 (2019).
3. S.A. Khairallah, A.T. Anderson, A. Rubenchik, W.E. King, “Laser powder-bed fusion additive manufacturing: Physics of complex melt flow and formation mechanisms of pores, spatter, and denudation zones,” *Acta Materialia* 108, 36-45 (2016).
4. W.E. King, A.T. Anderson, R.M. Ferencz, N.E.Hodge, C. Kamath, S.A. Khairallah, and A.M. Rubenchik, “Laser powder bed fusion additive manufacturing of metals: physics, computational and materials challenges,” *Appl. Phys. Rev.* 2, 041304 (2015).
5. Y. Kok, X.P. Tan, P. Wang, M.L.S. Nai, N.H. Loh, E. Liu, S.B. Tor, “Anisotropy and heterogeneity of microstructure and mechanical properties in additive manufacturing: A critical review,” *Materials and Design* 139, 565-586 (2018).
6. R. Cunningham, R., Narra, S. P., Montgomery, C., J. Beuth, and A.D. Rollett, “Synchrotron-based X-ray microtomography characterization of the effect of processing variables on porosity formation in laser power-bed additive manufacturing of Ti-6Al-4V,” *JOM*, 69(3), 479-484, 2017.
7. C. Zhao, K. Fezzaa, R.W. Cunningham, H. Wen, F. De Carlo, L. Chen, A.D. Rollett, and T. Sun, “Real-time monitoring of laser powder bed fusion process using high-speed X-ray imaging and diffraction,” *Scientific Reports*, 7(1), 3602 (2017).
8. W.J. Sames, F.A. List, S. Pannala, R.R. Dehoff, and S.S. Babu, “The metallurgy and processing science of metal additive manufacturing,” *International Materials Reviews*, 61(5), 315-360 (2016).
9. J.J. Lewandowski, & M. Seifi, “Metal additive manufacturing: a review of mechanical properties,” *Annual Review of Materials Research*, 46, 151-186 (2016).
10. A.B. Spierings, T.L. Starr, K. Wegener, “Fatigue performance of additive manufactured metallic parts,” *Rapid Prototyping Journal* 19(2), 88-94 (2013).
11. S. Tamas-Williams, P. J. Withers, I. Todd, and P.B. Prangnell, “The influence of porosity on fatigue crack initiation in additively manufactured titanium components,” *Scientific Reports* 7, 7308 (2017).
12. D. Kong, C. Dong, X. Ni, X. Li, “Corrosion of metallic materials fabricated by selective laser melting,” *Nature Materials Degradation* 3(24), 1-13 (2019).
13. G. Sander, J. Tan, P. Balan, O. Gharbi, D.R. Feenstra, L. Singer, S. Thomas, R.G. Kelly, J.R. Scully, and N. Birbillis, “Corrosion of additively manufactured alloys: A review,” *Corrosion* 74(12), 1318-1350 (2018).
14. Q.Y. Lu and C.H. Wong, “Application of non-destructive testing techniques for post-process control of additively manufactured parts,” *Virtual and Physical Prototyping* 12(4), 301-321 (2017).

15. L. Meng, B. Mcwilliams, W. Jarosinski, H.-Y. Park, Y.-G. Jung, J. Lee, and J. Zhang, "Machine learning in additive manufacturing: A review," *JOM* 72(6), 2363-2377 (2020).
16. L. Meng, J. Zhang, "Process design of laser powder bed fusion of stainless steel using a Gaussian process-based machine learning model," *JOM* 72(1), 420-428 (2020).
17. X. Qi, G. Chen, Y. Li, X. Cheng, C. Li, "Applying neural-network-based machine learning to additive manufacturing: Current applications, challenges, and future perspectives," *Engineering* 5, 721-729 (2019).
18. C. Goberta, E. W. Reutzelb, J. Petrichc, A. R. Nassarb, S. Phohac, "Application of supervised machine learning for defect detection during metallic powder bed fusion additive manufacturing using high resolution imaging," *Additive Manufacturing* 21, 517-528 (2018).
19. A. Thompson, I. Maskery, R. Leach, "X-ray computed tomography for additive manufacturing: A review," *Measurement Science and Technology* 27, 072001 (2016).
20. J. Raplee, A. Plotkowski, M.M. Kirka, R. Dinwiddie, A. Okello, R.R. Dehoff, and S.S. Babu, "Thermographic microstructure monitoring in electron beam additive manufacturing," *Scientific Reports* 7, 43554 (2017).
21. S.D. Holland and R.S. Reusser, "Material evaluation by infrared thermography," *Annual Reviews of Materials Research* 46, 287-303 (2016).
22. A. Heifetz, D. Shribak, T. Liu, T.W. Elmer, P. Kozak, S. Bakhtiari, B. Khaykovich, W. Cleary, "Pulsed thermal tomography nondestructive evaluation of additively manufactured reactor structural materials," *Transactions of the American Nuclear Society* 121(1), 589-591 (2019).
23. Q. Luo, B. Gao, W.L. Woo, Y. Yang, "Temporal and spatial deep learning network for infrared thermal defect detection," *NDT&E International* 108, 102164 (2019).
24. J.E. Siegel, M.F. Beemer, S.M. Shepard, "Automated non-destructive inspection of fused filament fabrication components using thermographic signal reconstruction," *Additive Manufacturing* 31, 100923 (2020).
25. X. Zhang, J. Saniie, A. Heifetz, "Neural Learning Based Blind Source Separation for Detection of Material Defects in Pulsed Thermography Images," to appear in *Proceedings of IEEE International Conference on Electro-Information Conference (EIT)*, (2020).
26. C.S. Kim, "Thermophysical properties of stainless steels," *ANL-75-55* (1975).
27. D.G. Farwick and R.N. Johnson, "Thermophysical properties of selected wear-resistant alloys," *HEDL-TME* 79-6 (1980).
28. G. Hinton, T. Sejnowski (Editors), "Unsupervised Learning: Foundations of Neural Computation," *MIT Press*. Boston, MA (1999).
29. R. Xu, D. Wunsch, "Survey of clustering algorithms," *IEEE Transactions on Neural Networks* 16(3), 645-678 (2005).
30. K. Sikka, G. Sharma, "Discriminatively trained latent ordinal model for video classification," *IEEE Transactions on Pattern Analysis and Machine Intelligence* 25(8), 1829 - 1844 (2017).

31. Z. H. Lai, Y. Xu, Q. C. Chen, J. Yang, D. Zhang, "Multilinear sparse principal component analysis," *IEEE Transactions on Neural Networks and Learning Systems* 25(10), 1942-1950 (2014).
32. J. Lucke, AS. Sheikh, "Closed-Form EM for Sparse Coding and Its Application to Source Separation," *Proceedings of International Conference on Latent Variable Analysis and Signal Separation*, 213–221 (2012).
33. Y. Bengio, A. Courville and P. Vincent, "Representation Learning: A review and new perspectives," *IEEE Transactions on Pattern Analysis and Machine Intelligence* 35(8), 1798 - 1828 (2013).
34. W. Q. Fan and W. S. Xiao, "Image denoising based on wavelet thresholding and Wiener filtering in the wavelet domain," *The Journal of Engineering*, 6012-6015 (2019).
35. N Rajic, "Principal component thermography for flaw contrast enhancement and flaw depth characterisation in composite structure," *Composite Structures*, 58(4): 521-528. (2002).
36. V. Strela and A. T. Walden, "Signal and image denoising via wavelet thresholding: Orthogonal and biorthogonal, scalar and multiple wavelet transforms," *Imperial College, Statistics Section*, London, U.K., Tech. Rep. TR-98-01 (1998).
37. X. Zhang, T. Gonnot, J. Saniie, "Real-time face detection and recognition in complex background," *Journal of Signal and Information Processing* 8, 99-112 (2017).
38. A. Hyvärinen. "The fixed-point algorithm and maximum likelihood estimation for independent component analysis," *Journal of Neural Processing Letters* 10(1), 1–5 (1999).
39. N. Y. Wang, T. S. Yao, J. D. Wang and D. Y. Yeung, "A probabilistic approach to robust matrix factorization," *European Conference on Computer Vision*, 126-139 (2012).



Nuclear Science and Engineering (NSE) Division

Argonne National Laboratory

9700 South Cass Avenue, Bldg. 208

Argonne, IL 60439

www.anl.gov



Argonne National Laboratory is a U.S. Department of Energy
laboratory managed by UChicago Argonne, LLC